THE JOURNAL OF
PHYSICAL CHEMISTRY
LETTERS
A JOURNAL OF THE AMERICAN CHEMICAL SOCIETY

Temperature-Dependent Lattice Dynamics and Vibration Effects in Cs_2UCl_6: Insights from DFT and Machine Learning Analysis

Published as part of The Journal of Physical Chemistry Letters special issue "Photophysics of Materials".

Yibo Wang, Kun Yang,* Xueyu Zhang, Feida Chen, and Xiaobin Tang*

Cite This: *J. Phys. Chem. Lett.* 2025, 16, 9656−9663

Read Online

ACCESS | Metrics & More | Article Recommendations

ABSTRACT: Uranium-based materials show great promise as scintillators in ultraprecise detector application owing to their strong radiation stopping capabilities and excellent spatial resolution. However, the excited-state-driven ultrafast lattice dynamics of uranium compounds remain insufficiently understood. In this study, the lattice dynamics of Cs_2UCl_6 were investigated through density functional theory (DFT) and machine learning (ML). The results indicate that $[UCl_6]^{4-}$ predominates at high frequencies (>100 cm^{-1}), which interacts with Cs at low frequencies (<100 cm^{-1}). The asymmetric stretching (ω_0) and bending (ω_1) octahedral vibrations of $[UCl_6]^{4-}$ exhibit a high degree of temperature sensitivity, while the ML results indicate nonlinear synergistic effects, especially the disorder of bond angles resulting in the oscillation of the potential energy surface. These findings suggest that the phonon scattering is attributable to the structure distortion of the $[UCl_6]^{4-}$ complex under asymmetric low-frequency bending vibration, thereby providing theoretical insight for the lattice dynamics behavior and spectral regulation in Cs_2UCl_6.

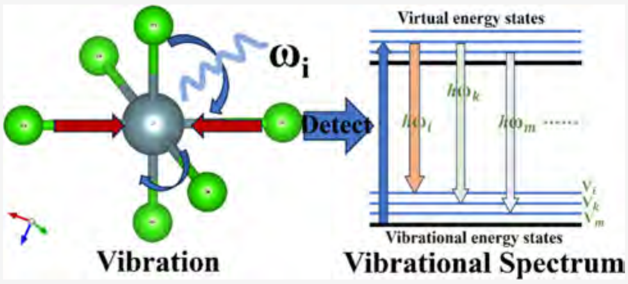

Halide perovskites (HPs) have attracted broad attention due to their excellent optoelectronic properties, including high quantum yield, superior carrier mobility, and tunable bandgaps,[1−3] which impart unique properties for their applications in photovoltaic devices, light-emitting diodes (LEDs), and high-sensitivity X-ray detectors.[4−6] U-based perovskites with B-site substitution have attracted considerable attention because of their ultrahigh power stopping capability and ultralow dose detection stability. In particular, their lattice symmetry can be adjusted to achieve low-temperature superconductivity.[7−9] Studies have shown that photoelectronic properties strongly depend on their unique electronic structure and lattice dynamics, which govern carrier transport, recombination processes, and phase stability.[10−12] However, the relationship between the photophysical and material properties of the U-based perovskites remain unclear. The "soft" nature of the perovskite octahedral framework facilitates strong exciton−phonon coupling, indicating a complex interaction between the electronic dynamics process and lattice vibrations and further affecting the optical properties of the materials.

The potential nexus between the lattice dynamics and the optoelectrical properties of HPs has been extensively studied. Previous studies have shown that the coherent vibrational movements might induce polaron formation and structural reorganization,[13,14] enhancing absorption and increasing non-radiative energy dissipation. The reason can be attributed to the fact that the unique structure of the perovskite leads to a close interaction between its photoelectric properties and phonon behavior. For instance, in Pb−I systems, such as $CsPbI_3$, $MAPbI_3$ and $FAPbI_3$, Pb−I based perovskites have been extensively investigated as representative materials owing to their favorable bandgap properties, which indicate there are symmetrical or asymmetrical vibrations inside the perovskite octahedron. Giustino et al. combined density functional theory (DFT) and Raman to provide an approach to investigate the vibrational behavior of $MAPbI_3$, finding that the internal mechanism corresponds to the bending and stretching behaviors of the Pb−I framework at low frequencies, directly mediating polaron stabilization.[15] For $CsSnI_3$ system, this type of lattice vibration induces anharmonic interactions between the Cs and iodine cages, resulting in Sn−I bond stretching and an unusual increase in the band gap.[16] Similar studies indicated that anharmonicity further induces localized lattice distortion

Received: July 6, 2025
Revised: August 17, 2025
Accepted: September 3, 2025

https://doi.org/10.1021/acs.jpclett.5c02071
J. Phys. Chem. Lett. 2025, 16, 9656−9663

of the octahedral structure and facilitate phase transitions in picoseconds.[17−19]

Recent experimental and theoretical studies have provided multiple methods for resolving complex lattice dynamics in perovskites. Ultrafast spectroscopic techniques, such as transient absorption (TA) and time-domain Raman (TD-Raman) spectroscopy, have facilitated the tracing of vibrations in perovskites.[20−22] The self-consistent phonon (SCPH) theory focuses on decomposing the effective phonon frequency with temperature dependence, thereby correcting the phonon dispersion relation, and combining transient X-ray characterization can solve the lattice dynamics at the picosecond and atomic scale.[17,23−26] Ab-initio molecular dynamics (AIMD) provides superior temporal resolution and captures dynamic evolution to perform static calculations.[27,28] An integrated theoretical-experimental framework was established to elucidate lattice dynamics, providing a foundation for investigating phonon interactions in uranium-based perovskite materials.

Our previous studies synthesized a highly pure Cs_2UCl_6 crystal, which can be prepared as a single crystal and has a temperature stability up to 275 °C. The MOF and Cs_2UCl_6 composite can maintain a stable state in an aqueous environment for approximately 72 h. Cs_2UCl_6 exhibited a fluorescent response as a scintillator in X-rays ranging from 10 to 50 keV and different excitation wavelengths (280, 330, and 360 nm). That implies the potential for further development and application of uranium-containing materials in functionalization, particularly the high stopping-power capability conferred by its high atomic number. However, there are Rashba effects in $[UCl_6]^{4-}$ under variable excitation energies, suggesting the wavelength-dependent full width at half-maximum (fwhm) broadening.[29,30] In this study, we systematically investigated the lattice dynamics of Cs_2UCl_6 through a combination of DFT with machine learning (ML) methods. The velocity autocorrelation function (VACF) and velocity density of states (VDOS) were employed as approximate equivalents to Raman spectroscopy, enabling the detection of potential vibrational modes that are overlooked in experimental studies. The lattice dynamics of the system and the trends in phonon evolution were obtained from normal mode (NM) and ML calculations. The result resolves three characteristic vibrations that dominate the lattice response in Cs_2UCl_6, indicating that the lattice dynamics are temperature-dependent. The study provides fundamental theoretical insights into the lattice dynamics of Cs_2UCl_6 for strategically modulating its optical properties.

DFT Calculations. All DFT calculations were performed using the *Vienna Ab initio Simulation Package* (VASP) code[31,32] based on a 2 × 1 × 1 supercell. The projector augmented wave (PAW) pseudopotential was employed in the reciprocal space, and the exchange-correlation effects were treated by using the generalized gradient approximation (GGA) with the Perdew−Burke−Ernzerhof (PBE) functional. The DFT+U method and Spin−orbit coupling (SOC) was applied for the strong correlation effects of the uranium f-orbital electrons, along with van der Waals (DFT-D3). The U-J value was set to 0.5 eV, consistent with our previous study result.[30] Structural optimization was conducted under a cutoff of 600 eV with the Brillouin zone sampled set as 2 × 2 × 1. The convergence criteria reached 0.01 eV/Å and 10^{-8} eV/Å for AIMD calculations and NM calculations, respectively.

AIMD Calculation Details. All AIMD calculations were conducted at temperatures of 75, 200, 298, 400, and 500 K. The simulation temperature limit was set at 500 K, based on the decomposition temperature of Cs_2UCl_6 from our previous work.[30] A 2 ps equilibration relaxation was implemented prior to the 5 ps calculations, and the first 500 frames were discarded to ensure thermal equilibrium of the atomic system. The time step was set to 1 fs/step. The VACF was obtained by calculating the atomic velocity around the lattice sites, which can be expressed as

$$C_{vv}(t) = \frac{1}{N}\sum_{i=1}^{N}\langle \mathbf{v}_i(t)\cdot\mathbf{v}_i(0)\rangle \tag{1}$$

where N is the number of atoms and $\mathbf{v}_i(t)$ represents the velocity of the ith atom at time t. The discrete-time form in AIMD can be further added with the time step (Δt), M represents the total number of steps, and k is the delayed steps, which can be expressed as

$$C_{vv}(k\Delta t) = \frac{1}{M-k}\sum_{m=1}^{M-k}\left[\frac{1}{N}\sum_{i=1}^{N}\mathbf{v}_i(m\Delta t)\cdot\mathbf{v}_i((m+k)\Delta t)\right] \tag{2}$$

VDOS is the distribution of the vibrational mode frequency ω and can be obtained through the Fourier transform of VACF, which can represent the atomic vibration density of states:

$$g(\omega) = \frac{1}{2\pi}\int_{-\infty}^{\infty} C_{vv}(t)e^{-i\omega t}\,\mathrm{d}t \tag{3}$$

According to eq 3, the formula can be further expended as the entropy value

$$S = k_{\mathrm{B}}\int_0^{\infty}\left[\frac{\hbar\omega}{k_{\mathrm{B}}T}\frac{1}{e^{\hbar\omega/k_{\mathrm{B}}T}-1} - \ln(1-e^{-\hbar\omega/k_{\mathrm{B}}T})\right]g(\omega)\,\mathrm{d}\omega \tag{4}$$

where k_B is the Boltzmann constant and $\hbar$ represents the reduction of Planck's constant. The logic behind the VACF and VDOS calculations is illustrated in Figure 1(a).

ML Calculations. ML was employed to examine the relationship between the thermal vibration and the frequency shift. The number of calculated temperature points increased from 5 to 22. The time step was set in the same manner as the

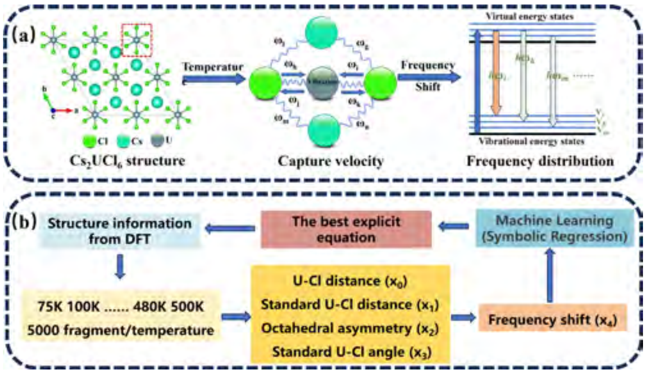

Figure 1. (a) Schematic of the execution logic of VACF and VDOS calculations. The blue wavy lines represent the vibrations between atoms, and the arrows are randomly selected to represent different vibration directions corresponding to different vibration frequencies. Here V_i, V_k, and V_m represent the different vibration energy levels. (b) Schematic of the workflow for the ML process.

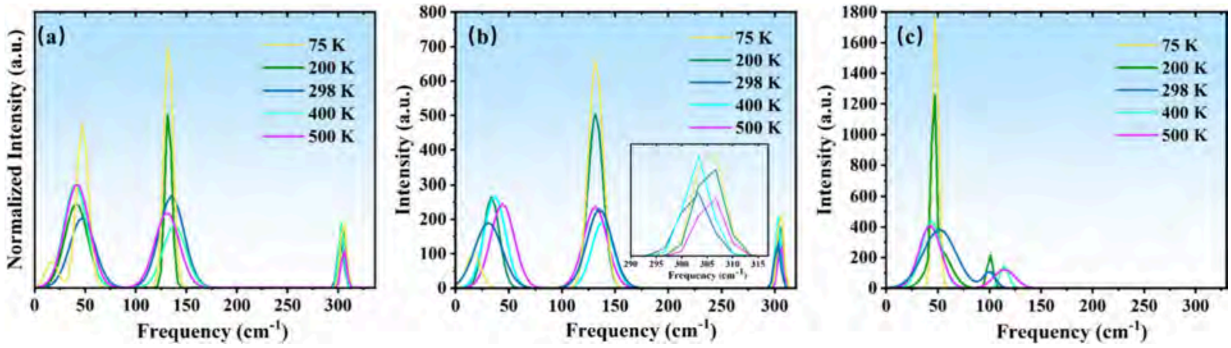

Figure 2. (a) Total VDOS plot of Cs_2UCl_6 and VDOS plots of (b) $[UCl_6]^{4-}$ pair and (c) Cs atoms at 75, 200, 298, 400, and 500 K.

AIMD setting (1 fs/step). All structures (5000 frames) at each temperature point will be extracted and subjected to Fourier transform analysis to identify their corresponding main frequencies, including 6 groups of the U−Cl distance and 15 groups of the U−Cl angle. These frequencies will be organized and stored in the time series file corresponding to the temperature point, which will be used in the subsequent equation fitting of symbolic regression. The four object arguments were selected as x_0, x_1, x_2, and x_3, representing the mean of U−Cl distance, the standard deviation of U−Cl distances, octahedral asymmetry (max distance-min distance), and U−Cl angle variation (standard deviation), respectively. Moreover, the objective function was built to describe the frequency shift ($\Delta\omega$). ML is employed to fit the symbolic regression equation, thereby establishing the mathematical relationship between the four aforementioned independent variables and the frequency shift. This process imposes no restrictions on mathematical operations and is designed to approach the actual value of the frequency shift within 100 iterations. The time series of the average U−Cl bond length in each structure was obtained as the "mean-distance" to eliminate the static bond length offsets and retain the dynamic vibration components. The bond angles were represented by Cl−U−Cl combinations within 90°, and the standard deviations were analyzed. Finally, an explicit equation was obtained through fitting. The workflow is illustrated in Figure 1(b).

The VDOS results for Cs_2UCl_6 from 75 to 500 K were derived from the AIMD calculations, as shown in Figure 2(a). Three of the main vibrational modes were located in the ranges of 40.37−47.36 cm^{-1} (ω_0), 131.52−138.16 cm^{-1} (ω_1), and 303.28−306.78 cm^{-1} (ω_7). The results found that ω_0 and ω_1 modes exhibit a pronounced sensitivity to temperature fluctuations, as evidenced by their intensity changes, whereas ω_7 shows relatively low sensitivity to temperature changes. The low-frequency ω_0 decreased by 50.04% as the temperature increased from 75 to 200 K and sustained a reduction of 17.7% at 298 K relative that at 200 K. However, a significant recovery occurred when the temperature reached 400 and 500 K, resulting in intensity increases of 50.27% and 50.41%, respectively, compared with those at 298 K. A substantial and irregular frequency shift was measured at 6.99 cm^{-1} with broadening of the fwhm until 500 K. The ω_1 mode possessed a greater vibration intensity than ω_0 and ω_7, which displayed a monotonic intensity reduction with an increase in temperature, accompanied by a smaller frequency red shift of 6.64 cm^{-1} in comparison to ω_0. The high-frequency ω_7 mode maintained remarkable thermal stability, with minimal changes in frequency of 306.65−303.29 cm^{-1}. The VDOS of ω_7 exhibited a similar trend with the ω_0 mode. The initial intensity of ω_1 decreased with rising temperature up to 298 K, as well as a notable reversal in intensity occurring at 400 K, which is the same as an intensity recovery of ω_7 occurring at 500 K. The nonmonotonic behavior remained constrained within a narrow variation range compared to the ω_0 and ω_1 modes, suggesting a delicate balance between the phonon population effects and the anharmonic coupling in the $[UCl_6]^{4-}$ framework.

The lattice dynamics of the octahedra in Cs_2UCl_6 were studied with $[UCl_6]^{4-}$ and Cs atoms were separately discussed to explore the source of the contributions. Figure 2(b) shows that the $[UCl_6]^{4-}$ vibrations manifest as two dominant peaks at ω_1 and ω_7. Despite the vibrational frequency close to ω_0, the primary intensity contributor to the frequency at ω_0 comes from the Cs vibrations according to Figure 2(c), especially when temperature <200 K, which exhibits higher intensities than the $[UCl_6]^{4-}$ vibrations. The temperature-dependent frequency shifts of $[UCl_6]^{4-}$ and Cs are summarized in Table 1. The results show that a similar quadratic function frequency shift occurred in $[UCl_6]^{4-}$ and Cs at ω_0, apart from the specific frequency at 16.34 cm^{-1}. The transition point of the nonlinear changes was located at 298 K, suggesting an exchange of the dominant mechanism. Both $[UCl_6]^{4-}$ and Cs underwent a pronounced fwhm broadening and an intensity reduction under the thermal activation of multiple vibrational states in the vicinity of ω_0. The maximum and minimum fwhm variation rates and intensity variation rates of $[UCl_6]^{4-}$ between 200 and 298 K are 43.98% and 28.56%, respectively, while those for the Cs atoms are 78.9% and 78.41%, respectively, between 75 and 298 K, respectively. The results show that the Cs atoms exhibited a greater sensitivity to temperature than $[UCl_6]^{4-}$ in the ω_0 mode. A group of phonon interactions of $[UCl_6]^{4-}$ and Cs atoms at low frequency exhibited a potential anharmonic effect with changes in temperature. The vibration behavior of the dominant mechanism is presented in the discussion.

Table 1. Main Peak Frequency Distributions (cm^{-1}) of ω_0 at Different Temperatures

	T (K)				
Atoms	75	200	298	400	500
$[UCl_6]^{4-}$	16.801	33.708	30.298	37.142	44.281
Cs	47.213	47.213	51.830	43.260	42.810

Both $[UCl_6]^{4-}$ and Cs contributed to the vibration at ω_1 mode. However, according to intensity analysis, the contribution of the Cs atoms was nearly negligible, with the

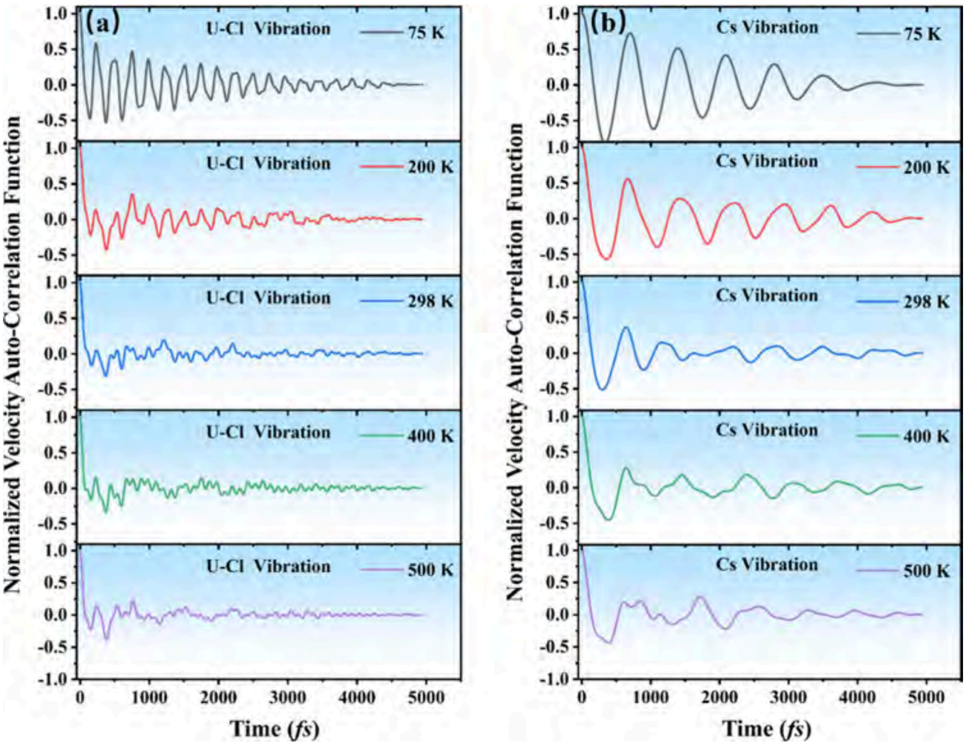

Figure 3. VACF comparison of (a) the $[UCl_6]^{4-}$ pair and (b) Cs atoms at 75, 200, 298, 400, and 500 K.

predominant vibration source being the octahedron composed of U−Cl. The ω_1 mode of $[UCl_6]^{4-}$ displays strong temperature dependence, with its intensity decreasing by 39.1% from 75 to 200 K, followed by 59.6% at 298 K. The vibration intensity monotonically decreased until 400 K, which can be attributed to thermal decoupling between U and Cl, consistent with the VDOS tendency of Cs_2UCl_6. The high vibration frequency of $[UCl_6]^{4-}$ was located at 303−306 cm^{-1}, which is close to the ω_7 mode. The inset shown in Figure 2(b) illustrates that the relationship between temperature and vibration intensity exhibits a "U-shaped" nonlinear response, with the maximum vibration intensity occurring at 75 K and gradually decreasing at elevated temperatures up to 298 K. However, the vibrations strengthened when the temperature increased to 400 K, which agree with the phenomenon that occurred in the ω_1 mode at 500 K. The temperature range for calculating the density of states was increased to 500 K with a significantly abnormal increase in both ω_1 and ω_7 modes still observed. The reason can be attributed to thermal expansion of the structure. Furthermore, the sensitivity of ω_1 and ω_7 to lattice constant changes was significantly different according to the rate of intensity changes, demonstrating the complex anharmonic motion of Cs_2UCl_6 vibrations. Overall, the vibrations of Cs_2UCl_6 were predominantly governed by $[UCl_6]^{4-}$ octahedra at high frequencies, with low-frequency contributions mainly coming from the Cs atom vibrations.

VACF investigated the phonon lifetime of Cs_2UCl_6 for both $[UCl_6]^{4-}$ and Cs atoms. Figure 3(a) shows that the VACF curves of $[UCl_6]^{4-}$ at 75 K exhibit symmetric oscillations surrounding the equilibrium position, indicating that the vibration of $[UCl_6]^{4-}$ is predominantly governed by harmonic motion. This harmonic vibration is destroyed at 200 K with the oscillation amplitude decreases compared to 75 K, which is in agreement with the VDOS observed in Figure 2(b). A distinct transition point occurs at 298 K, where the VACF waveform evolves from sinusoidal to irregular vibration, indicating the breakdown of the harmonic motion and the onset of anharmonic effects. Quantitative analysis shows that the phonon lifetime of $[UCl_6]^{4-}$ was 2.19 ps at 298 K, which is shorter than the 3.125 ps at 75 K, and decreased to 1.525 ps as the temperature reached 500 K by assuming that the criterion of vibration lifetime was below 0.1 in the normalized amplitude. These data and the VDOS results suggest intensity reduction and frequency shifts, confirming that anharmonic interactions already occurred when the system temperature was above 298 K. The Cs vibrations maintained their harmonic features at 200 K, as shown in Figure 3(b). The nonlinear vibration occurred when the temperature reached 298 K, and the motion was maintained until 500 K. Figures 3(a) and (b) show that the vibration frequency of Cs atoms is substantially lower than that of $[UCl_6]^{4-}$ in the same time range. This result is consistent with the VDOS results, confirming that the Cs atoms exhibit the most significant effect at low frequencies. A comparison of the vibration results shows that although the vibrations exhibited nonlinear trends as the temperature rises, the phonon lifetime increased from 3.49 ps at 298 K to 4.16 ps at 400 K. Therefore, it can be concluded that the vibration enhancement of Cs after 400 K can be attributed to the extra thermal energy compensation due to the increase in the phonon lifetime.

Three NMs were obtained by using the finite difference method to resolve the transition behavior from harmonic to anharmonic and identify the origins of the vibration disturbance. The vibration frequencies were located at NM0 (49.01 cm^{-1}), NM1 (132.96 cm^{-1}), and NM7 (299.43 cm^{-1}), which were considerably close to the ω_0, ω_1, and ω_7 modes in VDOS. Figure 4(a) shows the atomic bond lengths and angles. Evidently, two sets of asymmetric stretching as well as changes in the bond angle of Cl−U−Cl in Cs_2UCl_6 at ω_0 are observed. $U-Cl_1$ and $U-Cl_2$ shortened the bond length, while the other

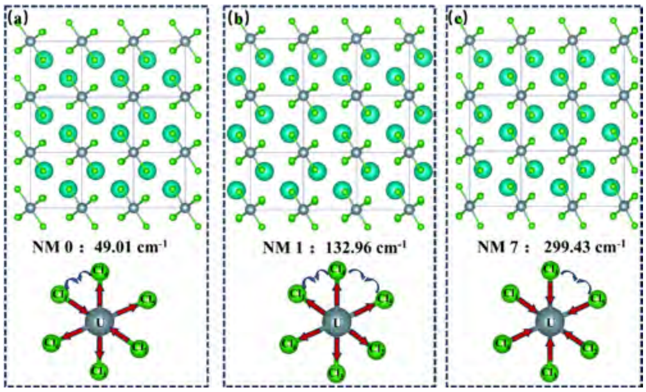

Figure 4. Three NMs of Cs_2UCl_6 at (a) 49.01 cm^{-1}, (b) 132.96 cm^{-1}, and (c) 299.43 cm^{-1}. The flat arrows indicate the direction of elongation and shortening of the apparent bond lengths, whereas the curved arrows indicate the direction of the atomic wobble.

U−Cl bonds were stretched at NM0. All the processes are accompanied by a decrease in the Cl_1−U−Cl_4 bond angle as presented in Table 2. Figure 4(b) shows that NM1 produces a vertical oscillation between two adjacent Cl atoms perpendicular to the two-dimensional plane. The bond angles of Cl_1−U−Cl_4 and Cl_1−U−Cl_3 changed significantly, with values of 79.39° and 100.61°, respectively, and the amplitude of the oscillation in the plane was approximately 10.61°. The oscillations of Cl_4−U−Cl_5 and Cl_4−U−Cl_6 were observed simultaneously, and the amplitude was approximately 8°, which was relatively lower than the rate of change between Cl_1−U−Cl_4 and Cl_1−U−Cl_3. Figure 4(c) shows a mixed vibrational mode of NM7; specifically, two groups of Cl atoms oscillate parallel to the plane around the U atom, whereas the $[UCl_6]^{4-}$ exhibits a symmetrical stretching. All bond lengths at NM7 decreased relative to those at the ground-state. The changes in bond angles mainly occurred between Cl_4−U−Cl_5 and Cl_4−U−Cl_6, with an oscillation amplitude of approximately 5.9°, which was smaller than the oscillation amplitude in NM1. In contrast, the bond length changes in NM1 were less than 0.03 Å, an ignored stretch compared to NM7. Overall, the vibrational mode of NM0 is a typical asymmetric vibration mode, whereas that of NM1 was generated by the oscillation of Cl atoms forming a plane with $[UCl_6]^{4-}$, which exhibited a mixed vibrational mode. Besides, the vibration peak of NM7 that was indicated in the experiment mainly originated from the symmetrical stretching behavior of $[UCl_6]^{4-}$.

Table 2. Statistics of Bond Length and Bond Angle Changes in Different NM Calculations

	Bond Length (Å) and Bond Angle (deg)			
	NM0 (49.01 cm^{-1})	NM1 (132.96 cm^{-1})	NM7 (299.43 cm^{-1})	Ground State
U−Cl_1	2.56576	2.6238	2.28982	2.61329
U−Cl_2	2.56569	2.6220	2.28994	2.61329
U−Cl_3	2.63323	2.64361	2.35734	2.61329
U−Cl_4	2.63342	2.64364	2.35727	2.61329
U−Cl_5	2.65213	2.62376	2.37851	2.61329
U−Cl_6	2.65218	2.62380	2.37846	2.61329
Cl_1−U−Cl_2	179.9917	179.9960	179.9986	180
Cl_3−U−Cl_4	179.9967	179.9981	179.9979	180
Cl_5−U−Cl_6	179.9938	179.9983	179.9984	180
Cl_1−U−Cl_4	**87.7354**	**79.3913**	90.0498	90
Cl_1−U−Cl_3	**92.2658**	**100.6071**	89.9520	90
Cl_4−U−Cl_5	89.3430	**82.1204**	**85.8105**	90
Cl_4−U−Cl_6	90.6515	**97.8789**	**94.1901**	90

A combined analysis of the VDOS and NM calculations revealed the distinct governing factors for each vibrational mode in Cs_2UCl_6. The current results suggest that the lattice dynamics of Cs_2UCl_6 are strongly temperature-dependent systems, which can be classified into the following based on three mechanisms: (1) thermal fluctuations of bond length induced by thermodynamic effects, (2) directional oscillations of the $[UCl_6]^{4-}$ bond angles, and (3) variations in the amplitude of asymmetric stretching of the $[UCl_6]^{4-}$ bonds. The dominant ω_1 and ω_7 modes of $[UCl_6]^{4-}$ are observed, indicating that intensity decreases with frequency blue-shift as the temperature increases. These results imply two primary mechanisms lead to the frequency shifts. First, thermal energy leads to a higher phonon occupation without significantly altering the lattice structure, which means the temperature is below the threshold of lattice rigidity. Second, thermal expansion occurred with increasing in bond lengths, causing phonon mode hardening and an increase in energy in the vibrational ensemble, as described by $\omega \propto \sqrt{k/m}$, where ω represents the frequency, k represents the force constant and m represents the effective mass. In addition, a significant reduction in the phonon lifetime of $[UCl_6]^{4-}$ implies a decrease in the Raman scattering cross-section, which accounts for the marked intensity reduction in the VDOS. Further NM1 calculations indicate that the bond angles with the largest oscillation amplitudes belong to the Cl_1−U−Cl_4 of Cl atoms. Thus, the primary source of the vibration intensity is the oscillation between U−Cl atoms.

Cs_2UCl_6 exhibited a mixed vibrational mode between the Cs atoms and $[UCl_6]^{4-}$ at ω_0, which must be discussed separately. The VACF results verify that the vibrational frequency of the Cs atoms around their equilibrium positions was significantly lower than that of $[UCl_6]^{4-}$ (Figure 3). A low-frequency vibration (16.34 cm^{-1}) was obtained with no specific vibration behavior being identified in the NM calculation. The $[UCl_6]^{4-}$ vibrational mode suggests an asymmetric stretching mode coupled with the smaller-amplitude oscillation of the Cl atom, thereby leading to higher vibration intensity at ω_0 than that at ω_7, which only exhibited bond stretching at 75 and 200 K. Therefore, this result suggests that the vibration at 16.34 cm^{-1} might be dominated by the stretching of the bonds that are not sensitive to temperature, which reduced the vibration frequency at 75 K. Furthermore, the coexistence of asymmetric stretching and oscillation between the $[UCl_6]^{4-}$ bonds rendered the frequency highly sensitive to temperature, resulting in the formation of anharmonic vibration in Cs_2UCl_6 and further causing significant frequency shift and fwhm broadening. A potential interaction between $[UCl_6]^{4-}$ and Cs atoms emerged when anharmonic interaction occurred in U−Cl, causing significant frequency shifts and vibrational damping in Cs_2UCl_6.

Based on the above analysis, the results indicate that understanding the behavior of U−Cl is crucial for elucidating the underlying phonon action mechanisms. As shown in Figure

1(a), the observed frequency shift and fwhm broadening suggest oscillation of the potential energy surface associated with NM0 and NM7, significantly impacting the energy transfer processes in the excited state. ML provides a further analysis of the mechanism of frequency shift. Equation 5 from symbolic regression revealed a nontrivial relationship between the structure distortion of octahedral and the vibrational frequency shifts, which enables identifying the dominant variables during $[UCl_6]^{4-}$ vibration. It is shown as

$$\Delta\omega = \left(\frac{x_1^{x_3}}{(x_3\cdot 2.165)^2\cdot 2.409}\right)^{-13.454} \qquad (5)$$

where x_1 (standard deviation of U−Cl distance) and x_3 (standard deviation of U−Cl angle) dominate the response. The square of $x_1^{x_3}$ indicates a synergistic effect between the bond length and the angle fluctuations. The numerator term rapidly increased as both x_1 and x_3 increased simultaneously, suggesting higher-order anharmonic coupling. The exponentiation amplifies bond length (x_1) effects via angular strain coupling (angular distortion from x_3) on the frequency shifts. The result resonates with the NM1 calculations showing that Cl_1−U−Cl_4 angle oscillations induce a wider fwhm than symmetric stretching in ω_7. An index of 2.409 indicates that the bond-angle disorder exhibits a nonlinear suppression effect on the frequency shift. The relationship between wavepacket oscillation and the frequency shift with temperature suggests changes in the potential energy surface. However, the asymmetry parameter x_2 was excluded from the optimal equation, implying that the static octahedral distortion contributes less to the dynamic angle fluctuations. This indicates that the degree of mismatch among different groups of U−Cl bond lengths and angles constitutes a key factor contributing to anharmonicity. The changes in the frequency shift and the equation of symbolic regression are listed in Figure 5. The fitting results indicate that symbolic regression does not entirely fit the actual frequency shift values above 300 K, and the ±1 σ error band encompasses 85% of the experimental shifts, validating its physical interpretability for the unique thermal response of uranium-based perovskites. The curve of symbolic fit exhibits a slight frequency shift at 200 K, which agrees with the VACF observed. The frequency shift increases significantly at 280 K, indicating that the degree of mismatch in U−Cl bond angles and bond lengths reaches its maximum. Moreover, the frequency shift displays oscillatory behavior with further temperature elevation. This suggests that within the 5 ps of our calculations, the potential energy surface of $[UCl_6]^{4-}$ in the excited state undergoes irregular fluctuations, exhibiting characteristic features of anharmonicity.

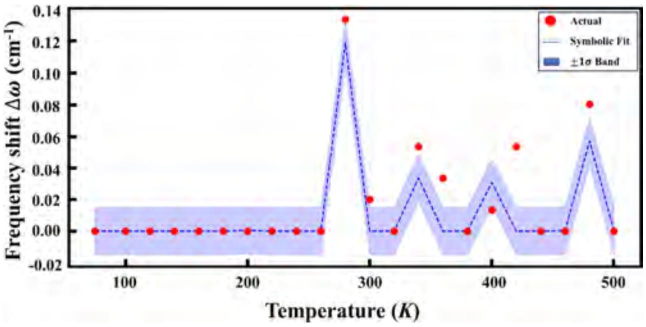

Figure 5. Frequency shift of $\Delta\omega$ with an increase in the temperature. The red dots represent the actual values, and the blue dashed line represents the symbolic regression function.

The temperature-dependent frequency distribution of Cs_2UCl_6 is observed below 150 cm^{-1}, which is significantly distinct from the frequencies of Pb−I based perovskites that typically occur below 100 cm^{-1}. The normal modes in Cs_2UCl_6 are predominantly characterized as mixture vibrations, especially asymmetric stretching and bending vibrations. There are also differences from a single normal mode that predominantly governs the vibrational behavior in Pb−I.[14] However, the nature of the lattice vibrations is not static. Previous studies have demonstrated that low-dimensional lattice structures, due to their quantum confinement effects, exert distinct influences on the formation of polarons, thereby significantly modulating the thermal carrier cooling process.[33−36] The zero-dimensional (0D) systems exhibited lower polaron binding energies compared to those in two-dimensional (2D) and three-dimensional (3D) structures.[37] This suggests that the polaron impact ratio of Cs_2UCl_6 under strong SOC is significantly higher than that of perovskite materials. Two primary strategies in literature review have been identified for modulating the luminescence of 0D perovskites. (1) Constructing isolated metal-halide octahedral lattices minimizes polaron-induced octahedral distortion, thereby suppressing low-frequency anharmonic vibrations and consequently enhancing both luminescence intensity and efficiency.[38,39] (2) In nonluminescent or weakly luminescent 0D perovskites, the formation of heterojunctions with 3D or 2D luminescent phases enhances the lattice rigidity of the composite material and facilitates more efficient energy transfer.[40] These findings provide valuable insights into optical modulation mechanisms based on the complex vibrational modes of Cs_2UCl_6 revealed in this study.

In summary, this study employed DFT and ML methods to resolve the lattice dynamics in Cs_2UCl_6, which provides a theoretical aspect to exhibit the dynamic behavior of phonon evolution with temperature. The results showed that the phonon behavior of Cs_2UCl_6 is affected by the variations in temperature, and the harmonic vibration lost equilibrium after the temperature reached 280 K. NM calculations confirm that the original anharmonic is asymmetric stretching and Cl oscillations, resulting in significant lattice scattering and frequency shifts. ML further identified that the interaction between the bond length and angle exhibits a subtle synergistic effect, which induced an oscillation of the potential energy surface within 5 *ps* at temperatures above 280 K. The results indicated that the degree of structural dispersion among different groups of U−Cl bond lengths and angles constitutes a key factor contributing to anharmonicity during the heating process. These findings indicate that a strong anharmonic lattice vibration increases the nonradiative recombination of Cs_2UCl_6, subsequently broadening the fwhm of the emission spectrum and reducing energy resolution as scintillators. Our research provides theoretical insights into the thermal lattice dynamics and fluorescence regulation strategies for uranium-based compounds, which could potentially broaden the range of scenarios in which poor uranium is functionally utilized.

■ ASSOCIATED CONTENT

Data Availability Statement

Data will be made available on request.

AUTHOR INFORMATION

Corresponding Authors

Kun Yang − *Department of Nuclear Science and Technology, Nanjing University of Aeronautics and Astronautics, Nanjing 211106, China; Key Laboratory of Advanced Nuclear Technology and Radiation Protection, Ministry of Industry and Information Technology, Nanjing 211106, China;* orcid.org/0000-0003-0040-3523; Email: kun.yang@nuaa.edu.cn

Xiaobin Tang − *Department of Nuclear Science and Technology, Nanjing University of Aeronautics and Astronautics, Nanjing 211106, China; Key Laboratory of Advanced Nuclear Technology and Radiation Protection, Ministry of Industry and Information Technology, Nanjing 211106, China;* orcid.org/0000-0003-3308-0468; Email: tangxiaobin@nuaa.edu.cn

Authors

Yibo Wang − *Department of Nuclear Science and Technology, Nanjing University of Aeronautics and Astronautics, Nanjing 211106, China*

Xueyu Zhang − *Department of Nuclear Science and Technology, Nanjing University of Aeronautics and Astronautics, Nanjing 211106, China*

Feida Chen − *Department of Nuclear Science and Technology, Nanjing University of Aeronautics and Astronautics, Nanjing 211106, China; Key Laboratory of Advanced Nuclear Technology and Radiation Protection, Ministry of Industry and Information Technology, Nanjing 211106, China;* orcid.org/0000-0002-1926-8563

Complete contact information is available at:
https://pubs.acs.org/10.1021/acs.jpclett.5c02071

Author Contributions

Y.W.: conceptualization, methodology, software, validation, formal analysis, investigation, data curation, writing−original draft, writing−review and editing. K.Y.: writing−original draft, writing−review and editing, funding acquisition. X.Z.: investigation. F.C.: writing−review and editing. X.T.: writing−original draft, supervision, project administration, funding acquisition.

Notes

The authors declare no competing financial interest.

ACKNOWLEDGMENTS

The author would like to acknowledge the financial support provided by the Postgraduate Research & Practice Innovation Program of Jiangsu Province (Grant No. KYCX23_0368). The Jiangsu Nature Science Foundation (BK20230898).

REFERENCES

(1) Mai, H.; Chen, D.; Tachibana, Y.; Suzuki, H.; Abe, R.; Caruso, R. A. Developing Sustainable, High-Performance Perovskites in Photocatalysis: Design Strategies and Applications. *Chem. Soc. Rev.* **2021**, *50* (24), 13692−13729.

(2) Min, X.; Xie, Q.; Wang, X.; Chen, M. Enhancing the Stability of Cesium Lead Iodide Perovskite Nanocrystals: Recent Progress. *Challenges and Opportunities. Surfaces and Interfaces* **2021**, *22*, 100870.

(3) Dey, A.; Ye, J.; De, A.; Debroye, E.; Ha, S. K.; Bladt, E.; Kshirsagar, A. S.; Wang, Z.; Yin, J.; Wang, Y.; et al. State of the Art and Prospects for Halide Perovskite Nanocrystals. *ACS Nano* **2021**, *15* (7), 10775−10981.

(4) Chen, J.; Zhang, W.; Pullerits, T. Two-Photon Absorption in Halide Perovskites and Their Applications. *Mater. Horizons* **2022**, *9* (9), 2255−2287.

(5) Li, Z.; Zhou, F.; Yao, H. H.; Ci, Z.; Yang, Z.; Jin, Z. Halide Perovskites for High-Performance X-Ray Detector. *Mater. Today* **2021**, *48*, 155−175.

(6) Di, J.; Chang, J.; Liu, S. F. Recent Progress of Two-dimensional Lead Halide Perovskite Single Crystals: Crystal Growth, Physical Properties, and Device Applications. *EcoMat* **2020**, *2* (3), 1−24.

(7) Bell, N. L.; Shaw, B.; Arnold, P. L.; Love, J. B. Uranyl to Uranium(IV) Conversion through Manipulation of Axial and Equatorial Ligands. *J. Am. Chem. Soc.* **2018**, *140* (9), 3378−3384.

(8) Zhang, Y.; Wang, X.; Xu, K.; Zhai, F.; Shu, J.; Tao, Y.; Wang, J.; Jiang, L.; Yang, L.; Wang, Y.; et al. Near-Unity Energy Transfer from Uranyl to Europium in a Heterobimetallic Organic Framework with Record-Breaking Quantum Yield. *J. Am. Chem. Soc.* **2023**, *145* (24), 13161−13168.

(9) Aishwarya, A.; May-Mann, J.; Raghavan, A.; Nie, L.; Romanelli, M.; Ran, S.; Saha, S. R.; Paglione, J.; Butch, N. P.; Fradkin, E.; Madhavan, V. Magnetic-Field-Sensitive Charge Density Waves in the Superconductor UTe_2. *Nature* **2023**, *618* (7967), 928−933.

(10) Guo, Z.; Wang, J.; Yin, W. J. Atomistic Origin of Lattice Softness and Its Impact on Structural and Carrier Dynamics in Three Dimensional Perovskites. *Energy Environ. Sci.* **2022**, *15* (2), 660−671.

(11) Folgueras, M. C.; Jin, J.; Gao, M.; Quan, L. N.; Steele, J. A.; Srivastava, S.; Ross, M. B.; Zhang, R.; Seeler, F.; Schierle-Arndt, K.; Asta, M.; Yang, P. Lattice Dynamics and Optoelectronic Properties of Vacancy-Ordered Double Perovskite Cs_2TeX_6 ($X = Cl^-, Br^-, I^-$) Single Crystals. *J. Phys. Chem. C* **2021**, *125* (45), 25126−25139.

(12) Seiler, H.; Zahn, D.; Taylor, V. C. A.; Bodnarchuk, M. I.; Windsor, Y. W.; Kovalenko, M. V.; Ernstorfer, R. Direct Observation of Ultrafast Lattice Distortions during Exciton-Polaron Formation in Lead Halide Perovskite Nanocrystals. *ACS Nano* **2023**, *17* (3), 1979−1988.

(13) Duan, H. G.; Tiwari, V.; Jha, A.; Berdiyorov, G. R.; Akimov, A.; Vendrell, O.; Nayak, P. K.; Snaith, H. J.; Thorwart, M.; Li, Z.; Madjet, M. E.; Dwayne Miller, R. J. Photoinduced Vibrations Drive Ultrafast Structural Distortion in Lead Halide Perovskite. *J. Am. Chem. Soc.* **2020**, *142* (39), 16569−16578.

(14) Park, M.; Neukirch, A. J.; Reyes-Lillo, S. E.; Lai, M.; Ellis, S. R.; Dietze, D.; Neaton, J. B.; Yang, P.; Tretiak, S.; Mathies, R. A. Excited-State Vibrational Dynamics toward the Polaron in Methylammonium Lead Iodide Perovskite. *Nat. Commun.* **2018**, *9* (1), 1−9.

(15) Pérez-Osorio, M. A.; Milot, R. L.; Filip, M. R.; Patel, J. B.; Herz, L. M.; Johnston, M. B.; Giustino, F. Vibrational Properties of the Organic-Inorganic Halide Perovskite CH3NH3PbI3 from Theory and Experiment: Factor Group Analysis, First-Principles Calculations, and Low-Temperature Infrared Spectra. *J. Phys. Chem. C* **2015**, *119*, 25703−25718.

(16) Patrick, C. E.; Jacobsen, K. W.; Thygesen, K. S. Anharmonic Stabilization and Band Gap Renormalization in the Perovskite $CsSnI_3$. *Phys. Rev. B-Condens. Matter Mater. Phys.* **2015**, *92* (20), 1−5.

(17) Yao, Z.; Cao, W.; Wang, Z.; Miao, L.; Shi, J.; Xiong, R. Anharmonic Phonon Renormalization and Thermoelectric Properties of $CsPbX_3$ (X = Cl, Br, and I): First-Principles Calculations. *Phys. Chem. Chem. Phys.* **2023**, *25* (38), 26236−26244.

(18) Marronnier, A.; Lee, H.; Geffroy, B.; Even, J.; Bonnassieux, Y.; Roma, G. Structural Instabilities Related to Highly Anharmonic Phonons in Halide Perovskites. *J. Phys. Chem. Lett.* **2017**, *8* (12), 2659−2665.

(19) Yan, S.; Wang, W.; Wang, C.; Chen, L.; Ai, X.; Xie, Q.; Cheng, G. Anharmonic Phonon Scattering Study in $MnPS_3$ crystal by Raman Spectroscopy. *Appl. Phys. Lett.* **2022**, *121*, No. 032203.

(20) Narra, S.; Jokar, E.; Pearce, O.; Lin, C. Y.; Fathi, A.; Diau, E. W. G. Femtosecond Transient Absorption Spectra and Dynamics of Carrier Relaxation of Tin Perovskites in the Absence and Presence of Additives. *J. Phys. Chem. Lett.* **2020**, *11* (14), 5699−5704.

(21) Kuramochi, H.; Tahara, T. Tracking Ultrafast Structural Dynamics by Time-Domain Raman Spectroscopy. *J. Am. Chem. Soc.* **2021**, *143* (26), 9699−9717.

(22) Berera, R.; van Grondelle, R.; Kennis, J. T. M. Ultrafast Transient Absorption Spectroscopy: Principles and Application to Photosynthetic Systems. *Photosynth. Res.* **2009**, *101* (2−3), 105−118.

(23) Filippi, U.; Toso, S.; Zaffalon, M. L.; Pianetti, A.; Li, Z.; Marras, S.; Goldoni, L.; Meinardi, F.; Brovelli, S.; Baranov, D.; Manna, L. Cooling-Induced Order-Disorder Phase Transition in CsPbBr 3 Nanocrystal Superlattices. *Adv. Mater.* **2025**, *37*, 2410949.

(24) Monacelli, L.; Bianco, R.; Cherubini, M.; Calandra, M.; Errea, I.; Mauri, F. The Stochastic Self-Consistent Harmonic Approximation: Calculating Vibrational Properties of Materials with Full Quantum and Anharmonic Effects. *J. Phys.: Condens. Matter* **2021**, *33* (36), 363001.

(25) Wang, Q.; Zeng, Z.; Chen, Y. Revisiting Phonon Transport in Perovskite $SrTiO_3$: Anharmonic Phonon Renormalization and Four-Phonon Scattering. *Phys. Rev. B* **2021**, *104* (23), 1−6.

(26) Panuganti, S.; Cuthriell, S. A.; Leonard, A. A.; Quintero, M. A.; Laing, C. C.; Guzelturk, B.; Zhang, X.; Chen, L. X.; Kanatzidis, M. G.; Schaller, R. D. Transient X-ray Diffraction Reveals Nonequilibrium Phase Transition in Thin Films of $CH_3NH_3PbI_3$ Perovskite. *ACS Energy Lett.* **2023**, *8* (1), 691−698.

(27) Yadav, V. K.; Chakraborty, H.; Klein, M. L.; Waghmare, U. V.; Rao, C. N. R. Defect-Enriched Tunability of Electronic and Charge-Carrier Transport Characteristics of 2D Borocarbonitride (BCN) Monolayers from: Ab Initio Calculations. *Nanoscale* **2019**, *11* (41), 19398−19407.

(28) Brunig, F. N.; Geburtig, O.; Canal, A. v.; Kappler, J.; Netz, R. R. Time-Dependent Friction Effects on Vibrational Infrared Frequencies and Line Shapes of Liquid Water. *J. Phys. Chem. B* **2022**, *126* (7), 1579−1589.

(29) Manchon, A.; Koo, H. C.; Nitta, J.; Frolov, S. M.; Duine, R. A. New Perspectives for Rashba Spin-Orbit Coupling. *Nat. Mater.* **2015**, *14* (9), 871−882.

(30) Wang, Y.; Yang, K.; Chen, F.; Qu, X.; He, Y.; Han, D.; Tang, X. Structural Stability and Photoluminescence Property of Cs_2UCl_6 Single Crystal Derived from Spent Nuclear Fuel. *Inorg. Chem.* **2025**, *64* (7), 3178−3187.

(31) Kresse, G.; Hafner, J. Ab Initio Molecular Dynamics for Liquid Metals. *Phys. Rev. B* **1993**, *47* (1), 558−561.

(32) Kresse, G.; Furthmüller, J. Efficiency of Ab-Initio Total Energy Calculations for Metals and Semiconductors Using a Plane-Wave Basis Set. *Comput. Mater. Sci.* **1996**, *6* (1), 15−50.

(33) Belessiotis, G. V.; Arfanis, M.; Kaltzoglou, A.; Likodimos, V.; Raptis, Y. S.; Falaras, P.; Kontos, A. G. Temperature Dependence of the Vibrational and Emission Spectra in the 0D Vacancy-Ordered Cs_2SnI_6 Perovskite. *Mater. Today Proc.* **2022**, *67*, 971−974.

(34) Biswas, S.; Zhao, R.; Alowa, F.; Zacharias, M.; Sharifzadeh, S.; Coker, D. F.; Seferos, D. S.; Scholes, G. D. Exciton Polaron Formation and Hot-Carrier Relaxation in Rigid Dion−Jacobson-Type Two-Dimensional Perovskites. *Nat. Mater.* **2024**, *23* (7), 937−943.

(35) Thouin, F.; Valverde-Chávez, D. A.; Quarti, C.; Cortecchia, D.; Bargigia, I.; Beljonne, D.; Petrozza, A.; Silva, C.; Srimath Kandada, A. R. Phonon Coherences Reveal the Polaronic Character of Excitons in Two-Dimensional Lead Halide Perovskites. *Nat. Mater.* **2019**, *18* (4), 349−356.

(36) Debnath, T.; Sarker, D.; Huang, H.; Han, Z. K.; Dey, A.; Polavarapu, L.; Levchenko, S. V.; Feldmann, J. Coherent Vibrational Dynamics Reveals Lattice Anharmonicity in Organic-Inorganic Halide Perovskite Nanocrystals. *Nat. Commun.* **2021**, *12* (1), 2629.

(37) Yin, J.; Maity, P.; De Bastiani, M.; Dursun, I.; Bakr, O. M.; Brédas, J. L.; Mohammed, O. F. Molecular Behavior of Zero-Dimensional Perovskites. *Sci. Adv.* **2017**, *3* (12), 2−9.

(38) Zhang, W.; Wei, J.; Gong, Z.; Huang, P.; Xu, J.; Li, R.; Yu, S.; Cheng, X.; Zheng, W.; Chen, X. Unveiling the Excited-State Dynamics of Mn^{2+} in 0D Cs_4PbCl_6 Perovskite Nanocrystals. *Adv. Sci.* **2020**, *7* (22), 2−9.

(39) Zhang, A.; Jin, J.; Xia, Z. Tunable Luminescence of Sb^{3+} Doped 0D Cs_4PbCl_6 Nanocrystals from Three Distinct Emission Centers. *Adv. Opt. Mater.* **2022**, *10* (19), 1−7.

(40) Zhong, C.-Y.; Li, L.; Chen, Q.; Jiang, K.-Z.; Li, F.-t.; Liu, Z.-Q.; Chen, Y. Enhanced Exciton-to-Mn^{2+} Energy Transfer in 3D/0D Cesium−Lead−Chloride Composite Perovskites. *Adv. Opt. Mater.* **2023**, *11* (4), 2−9.